

See discussions, stats, and author profiles for this publication at: <https://www.researchgate.net/publication/275660650>

Demonstration of Confined Electron Gas and Steep-Slope Behavior in Delta-Doped GaAs-AlGaAs Core-Shell Nanowire Transistors

ARTICLE *in* NANO LETTERS · MAY 2015

Impact Factor: 13.59 · DOI: 10.1021/acs.nanolett.5b00518 · Source: PubMed

CITATIONS

3

READS

71

12 AUTHORS, INCLUDING:



[Daniel Rudolph](#)

Technische Universität München

25 PUBLICATIONS 375 CITATIONS

SEE PROFILE



[Jonathan James Finley](#)

Technische Universität München

216 PUBLICATIONS 4,487 CITATIONS

SEE PROFILE



[Lincoln J Lauhon](#)

Northwestern University

182 PUBLICATIONS 10,646 CITATIONS

SEE PROFILE



[Gerhard Abstreiter](#)

Technische Universität München

786 PUBLICATIONS 17,801 CITATIONS

SEE PROFILE

Demonstration of Confined Electron Gas and Steep-Slope Behavior in Delta-Doped GaAs-AlGaAs Core–Shell Nanowire Transistors

S. Morkötter,^{*,†} N. Jeon,[‡] D. Rudolph,[†] B. Loitsch,[†] D. Spirkoska,[†] E. Hoffmann,^{†,||} M. Döblinger,[§] S. Matich,[†] J. J. Finley,[†] L. J. Lauhon,[‡] G. Abstreiter,^{†,||} and G. Koblmüller^{*,†}

[†]Walter Schottky Institut, Physik Department, and Center of Nanotechnology and Nanomaterials, Technische Universität München, Garching 85748, Germany

[‡]Department of Materials Science and Engineering, Northwestern University, Evanston, Illinois 60201, United States

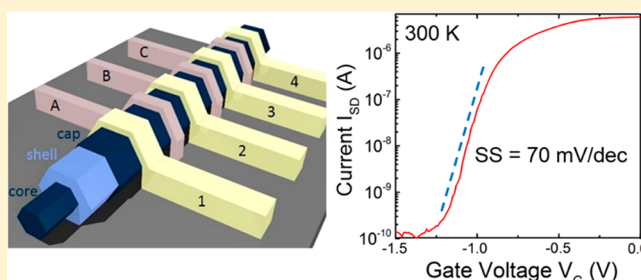
[§]Department of Chemistry, Ludwig-Maximilians-Universität München, Munich 81377, Germany

^{||}Institute for Advanced Study, Technische Universität München, Garching 85748, Germany

Supporting Information

ABSTRACT: Strong surface and impurity scattering in III–V semiconductor-based nanowires (NW) degrade the performance of electronic devices, requiring refined concepts for controlling charge carrier conductivity. Here, we demonstrate remote Si delta (δ)-doping of radial GaAs-AlGaAs core–shell NWs that unambiguously exhibit a strongly confined electron gas with enhanced low-temperature field-effect mobilities up to $5 \times 10^3 \text{ cm}^2 \text{ V}^{-1} \text{ s}^{-1}$. The spatial separation between the high-mobility free electron gas at the NW core–shell interface and the Si dopants in the shell is directly verified by atom probe tomographic (APT) analysis, band-profile calculations, and transport characterization in advanced field-effect transistor (FET) geometries, demonstrating powerful control over the free electron gas density and conductivity. Multigated NW-FETs allow us to spatially resolve channel width- and crystal phase-dependent variations in electron gas density and mobility along single NW-FETs. Notably, dc output and transfer characteristics of these n-type depletion mode NW-FETs reveal excellent drain current saturation and record low subthreshold slopes of 70 mV/dec at on/off ratios $>10^4$ – 10^5 at room temperature.

KEYWORDS: Delta-doped GaAs-AlGaAs core–shell nanowires, two-dimensional electron gas formation, field effect transistors, transport, atom probe tomography



The strong confinement of charge carrier gases in low-dimensional semiconductor heterostructures is a key enabling concept for the engineering of high-mobility carrier channels. This concept was pioneered in planar two-dimensional AlGaAs/GaAs and strained SiGe/Si heterostructures, whereby remote- or modulation-doped semiconductor heterojunctions enhance charge carrier mobility by the formation of a two-dimensional electron gas (2DEG) channel that is spatially separated from dopant impurities.^{1–6} As a result, these structures are test beds for innovative low-dimensional condensed matter physics that have enabled important discoveries, such as the integral and fractional quantum Hall effects,^{7,8} but also practical applications such as low-noise, high-frequency modulation-doped field effect transistors (MOD-FETs)^{9,10} and platforms for quantum computation.¹¹ Transferring this paradigm to a nanowire (NW) geometry is of extremely high interest for fundamental quantum transport investigations^{12,13} and for next-generation high-speed/low-power electronic switches.¹⁴ In particular, high-mobility III–V semiconductor nanowire field effect transistors (NW-FETs) can offer enhanced transconductance, superior electrostatic gate

control enabled by wrap-gate geometries, and vertical integrability on the Si platform, complying with the aggressive scaling of Si-based CMOS technology.^{14–21} As the conductivity of charge carriers in highly downscaled NW geometries is strongly limited by scattering at the NW surface and ionized impurities,^{15,22} the remote doping concept is particularly appealing here.

Remote doping has recently been explored in Si/Ge core–shell heterostructure p-channel NW-FETs,^{15,23–25} InGaAs/InP/InAlAs n-channel NW-FETs,²¹ and GaAs-AlGaAs core–shell NW-FETs.^{26,27} In the prototypical GaAs NW system, combined strategies for passivation and precise doping are extremely critical because surface states and residual impurities not only limit conductivity but even cause amphoteric behavior.^{28–30} Surface passivation by AlGaAs shells therefore provides an important means to suppress charge carrier scattering at the NW surface and to enable unobscured n-

Received: February 6, 2015

Revised: April 9, 2015

Published: April 29, 2015

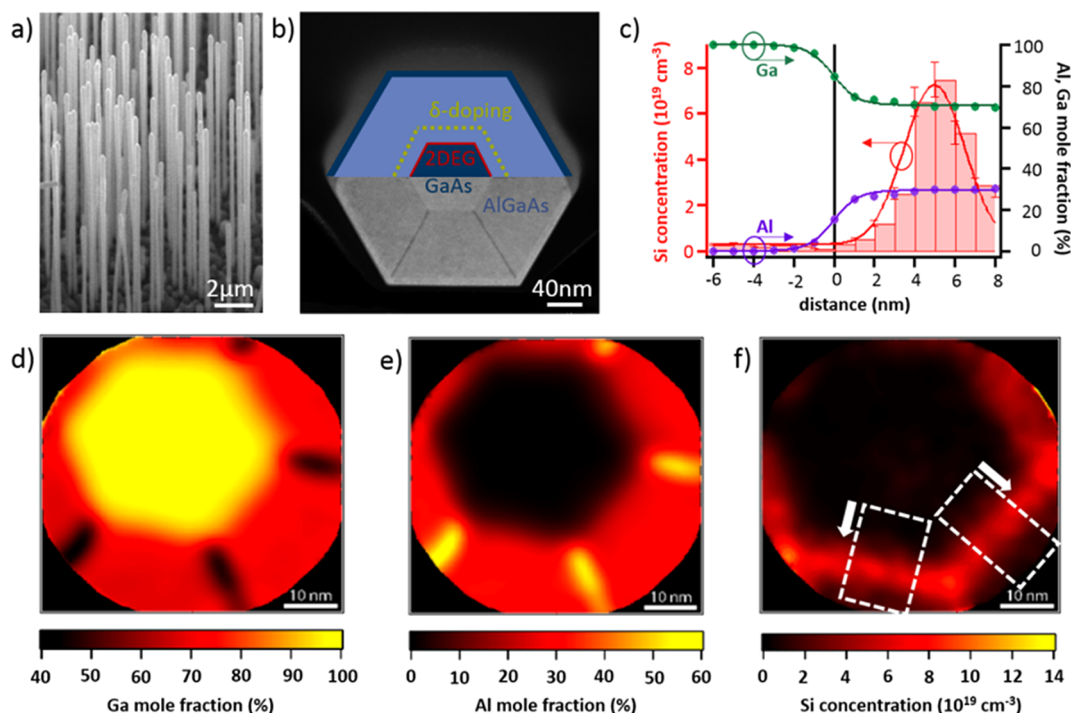


Figure 1. Growth and cross-sectional analysis of radial Si δ -doped GaAs-AlGaAs core-shell NWs. (a) SEM image of as-grown NWs on SiO₂/Si (111) substrates. (b) Cross-sectional HAADF-STEM image as well as APT elemental maps of Ga (d) and Al (e) revealing the complex AlGaAs shell structure with Al-enriched regions emerging from the corners of the hexagonal core; also, the δ -doping layer and the 2DEG are schematically indicated in (b). (f) End-view of the APT-measured Si doping distribution. (c) Corresponding averaged proximity histogram (see Methods) moving from core to shell within the regions indicated by the white boxes in (f). The core-shell interface is at 0 nm.

type conduction in the GaAs NW core with electron mobilities approaching bulk values for GaAs.^{31,32} However, electron transport obeyed bulk-like (3D) properties under the conditions probed in refs 31 and 32. The much desired low-dimensional free carrier gas properties have thus far been explored only in related quantum well (QW) structures embedded in GaAs-AlGaAs core-shell NWs.^{30,33} Whereas Jadcak et al. reported the formation of a defect-induced unintentional hole carrier gas,³⁰ we recently demonstrated intentional Si-doped electron gases in GaAs QWs in the form of 2D- and 1D-like channels via inelastic light scattering experiments and combined theoretical modeling.³³ A quasi-1D-like transport channel has been also suggested from zero-bias differential conductance measurements in planarized Si delta-doped GaAs-AlGaAs NWs, although resistivity measurements indicated decreased low-temperature conductivity as compared to room-temperature.³⁴ Despite all the extensive efforts devoted to remotely doped GaAs-AlGaAs core-shell NWs^{30–35} and related FET structures,^{26,27} a direct and unambiguous demonstration of the enhancement of low-temperature conductivity and electron mobility via reduction of ionized impurity scattering is still lacking. One of the major challenges in realizing functional remotely-doped core-shell NWs and NW-FETs is the difficulty in determining dopant incorporation and efficiency, which are key for the formation of well-confined high-mobility carrier gases.

Here, we directly report enhanced low-temperature conductivity and electron mobility in Si delta (δ)-doped GaAs-AlGaAs core-shell NW-FETs, demonstrating a reduction in ionized impurity scattering associated with the formation of a confined 2DEG adjacent to the core-shell heterointerface. By combining well-correlated atom probe tomography (APT),

band profile calculations and transport characterization, we demonstrate the excellent doping efficiency of the δ -doped layer, verified by good agreement between the as-measured doping densities and resulting free electron gas densities. Furthermore, these remotely doped core-shell NW-FETs exhibit excellent dc drain current saturation and record low subthreshold slopes as low as 70 mV/dec with on/off ratios of $>10^4$ – 10^5 at room-temperature.

The remotely Si δ -doped radial GaAs-AlGaAs core-shell NWs presented here were grown in a two-step process on prepatterned SiO₂/Si (111) substrates using molecular beam epitaxy (MBE). First, the [111]-oriented GaAs NW core was grown by a self-catalyzed (i.e., Ga droplet-mediated) vapor-liquid-solid growth process,³⁶ resulting in ~ 10 μ m long NWs that are slightly inversely tapered (i.e., with a gradual change in NW diameter from ~ 25 to ~ 90 nm from bottom to top as verified by atomic force microscopy). The crystal structure is nearly phase-pure zincblende (ZB) except for the top region, which contains many twin defects and stacking faults (see also Supporting Information, Figure S1). Subsequently, an epitaxial, nearly lattice-matched AlGaAs shell with a total thickness of ~ 80 nm was grown around the hexagonal {110} NW sidewall surfaces under conditions promoting radial growth³⁷ (see Methods). The shell was overgrown by an additional 10 nm thin GaAs cap layer to prevent the AlGaAs shell from oxidizing. A reference sample of smaller total diameter was also grown for atom probe tomography (APT) analysis consisting of a 20 nm thin AlGaAs shell and 5 nm thin GaAs cap (see Methods) on an identically grown GaAs core. For transistor measurements, two samples of different shell compositions were investigated, one with Al-content $x(\text{Al})$ of 0.15 (sample A) and one with $x(\text{Al})$ of 0.25 (sample B).

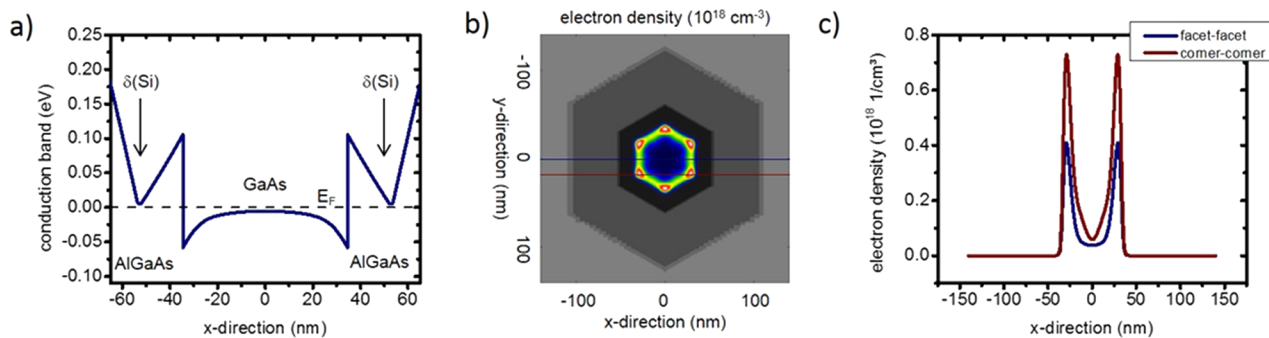


Figure 2. Band profile and free electron gas distribution. (a) Conduction band profile across the core-shell heterointerface using the given NW geometry and Si doping density; band bending occurs due to charge separation of the free electron gas at the GaAs-AlGaAs heterointerface and fixed ionized donors at the position of $\delta(\text{Si})$ (E_F is the Fermi level). (b) Free electron density distribution at the GaAs-AlGaAs core-shell interface exhibiting higher electron concentrations in the six corner regions (black and dark-gray illustrate the AlGaAs spacer and barrier regions, respectively). (c) Corresponding profile of the electron concentration across the main sidewall (blue) and corner (red) facets.

In each sample, a Si δ -doped layer was introduced during AlGaAs shell growth at a distance of 20 nm away from the core-shell interface (5 nm in the APT sample) by stopping the growth for 10 min under elemental Si supply. Growth conditions for the Si δ -doped layer around the six $\{110\}$ AlGaAs sidewall facets were adapted from optimized planar (110) AlGaAs/GaAs heterostructures to realize high-mobility electron gases with densities in the mid- 10^{11} cm^{-2} range.^{26,38} The δ -doped layer, which pins the Fermi level, thus separates the AlGaAs shell into a spacer layer (20 nm-wide region next to the core-shell interface where the free electron gas resides) and a barrier layer (remaining 60 nm-wide region adjacent to the shell surface). A representative scanning electron micrograph (SEM) and associated high angle annular dark field/scanning transmission electron microscopy (HAADF/STEM) cross-section of the as-grown core-shell NW heterostructure are shown in Figure 1(a,b) for sample B. These images confirm the epitaxial nature of the growth and reveal the symmetric shell growth around the NW core. The AlGaAs shell also exhibits the previously reported stripes of dark contrast propagating from $\{112\}$ corner facets across the entire shell region.³⁷ The Al content of these regions is twice that of the surrounding AlGaAs material (i.e., $x(\text{Al}) \sim 0.5$), as further confirmed by atom probe tomography (APT) maps of the Ga and Al compositional distribution in Figure 1(d,e).

Additional APT analysis was performed on the respective specimen to directly measure the position of and dopant concentration within the Si δ -doped layer (see also Methods^{39,40}). Figure 1(f) displays an APT-derived map of the Si δ -doping concentration, clearly showing the presence of a well-resolved Si dopant layer. By superposing the individual elemental APT maps of Figures 1(d–f), it is obvious that the Si dopants are spatially confined to a narrow (few nm wide) region within the AlGaAs shell at a distance away from the core-shell interface that matches well with the nominal spacer layer thickness. The slight asymmetry in the plots arises from a slight tilt of the probe-tip during the APT analysis. Figure 1(c) shows an averaged proximity histogram of the Si dopant distribution together with the measured molar fraction profiles for Al and Ga when moving across the core-shell heterointerface (regions marked by white boxes in Figure 1f); the average Si δ -doping density was determined to be $(\sim 6 \pm 1.6) \times 10^{19} \text{ cm}^{-3}$. The APT analysis thus enables a comparison of the measured Si doping densities with the resulting free electron

densities that can be simulated and accessed via transport characterization.

Using the accurate geometry and doping density data obtained from the STEM-HAADF and APT analyses, we derived the corresponding conduction band (CB) profile and free electron density by self-consistently solving the Schrödinger–Poisson equation using the nextnano³ device simulator.⁴¹ Panels a and b in Figure 2 show the CB profile across the NW heterostructure and the electron density distribution map near the GaAs-AlGaAs interface at a lattice temperature of 4K and zero bias (sample A). Similar profiles and electron density maps were also generated for sample B, because the geometry and doping density are fully equivalent (see Supporting Information, Figure S2). We note that, in the calculations of the CB profile, we disregarded here the locally higher Al-content in first order approximation in the six corner facets because they represent only a small (<5%) volume fraction of the AlGaAs shell. Gate-bias and Al-content-dependent simulations of the CB profile are further illustrated in the Supporting Information to account for the locally higher Al-content and to further describe the measured transport characteristics as shown below. Independent of these composition variations, the electron density map (Figure 2(b)) reveals a 1.8-fold enhancement in electron concentration at the six corners of the GaAs-AlGaAs shell interface compared to the adjacent sidewall facets (Figure 2(c)) due to the symmetry of the heterostructure.^{42,43} Taking the spatial extension of the electron gas into account, the Si doping density of $\sim 6 \times 10^{19} \text{ cm}^{-3}$ creates an equivalent two-dimensional electron gas (2DEG) density of 7.3×10^{11} and $4.1 \times 10^{11} \text{ cm}^{-2}$ at the corner and sidewall facets, respectively. Because the fraction of electron accumulation in the corner regions is $\sim 30\%$ of the total electron density—assuming an 80 nm-wide NW core diameter—the weighted total 2DEG density is $\sim 5.3 \times 10^{11} \text{ cm}^{-2}$. This can be directly compared to the total electron density derived from transconductance measurements (see below) to determine the Si δ -doping efficiency.

To characterize the electrical transport and transistor performance of the Si δ -doped GaAs-AlGaAs core-shell NWs, and thereby directly link electron gas formation with mobility enhancements, we fabricated single-wire NW-FETs. These consist of four annealed source/drain (S-D) contacts (using AuGe/Ni/Ti/Au) interspersed with three omega-shaped gates (using Ti/Au). The length of each individual gate is $L_G \sim 400 \text{ nm}$, whereas each pair of S-D contacts is separated by

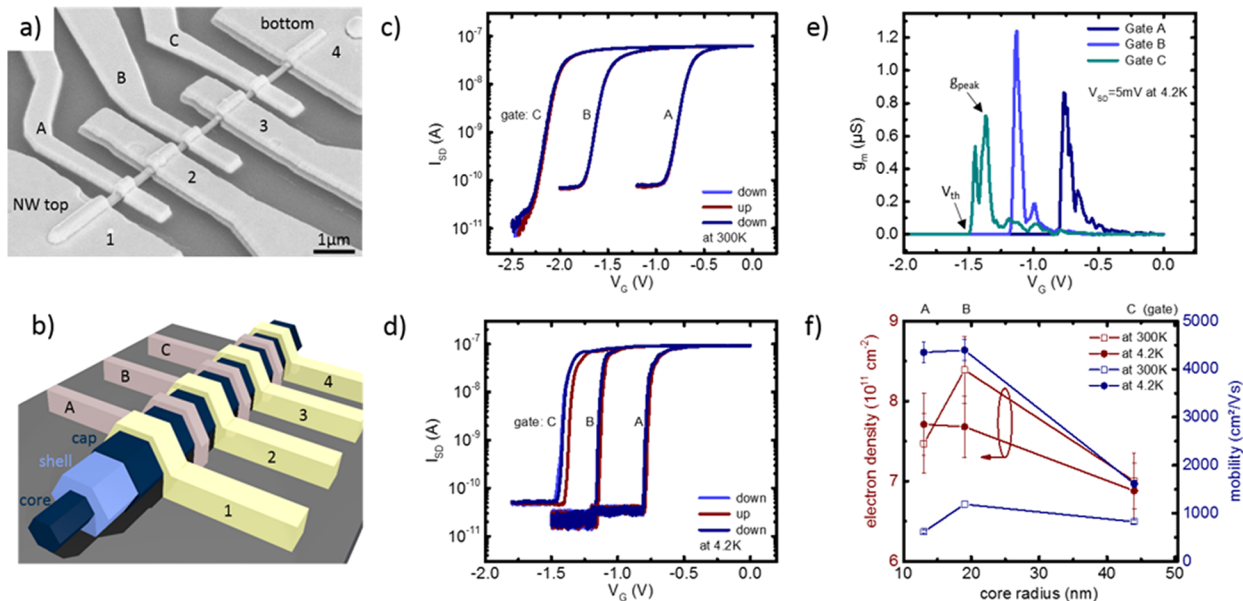


Figure 3. Position-dependent transfer characteristics and transport data along single NWs. (a, b) SEM image and schematic illustration of the fabricated NW-FET with four S-D contacts labeled 1–4 and three omega-shaped gates (A, B, C). I_{SD} – V_G transfer curves (at $V_{SD} = 5$ mV) for sample A [$x(\text{Al}) = 0.15$] at (c) 300 K and (d) 4.2 K as recorded at different positions along the NW (gates A–C); data was recorded by bidirectional sweeps of V_G (down-up-down). (e) Corresponding transconductance and threshold voltage V_{th} for the individual positions. (f) Extracted electron density and field-effect mobility plotted as a function of NW core radius at the different gates along the NW.

Table 1. Summary of NW-FET Characteristics Including a Comparison of Intrinsic NW Resistance (R_{NW}), Contact Resistance (R_C), Subthreshold Slope (SS), Current On/Off (I_{ON}/I_{OFF}) Ratio, and Drain-Induced Barrier Lowering (DIBL)^a

sample	$x(\text{Al})$	300 K		4.2 K (illuminated)		300 K	$V_{SD} = 1$ V	
		R_{NW} (k Ω)	R_C (k Ω)	R_{NW} (k Ω)	R_C (k Ω)	SS (mV/dec)	I_{ON}/I_{OFF}	DIBL (mV/V)
A	0.15	19.8 ± 3.6	28.7 ± 6.3	8.5 ± 3.3 (7 ± 1.1)	38.7 ± 30.4 (11.8 ± 6.6)	70–96	10^4 – 10^5	10–88
B	0.25	27.7 ± 2.3	36.7 ± 9.3	(15.6 ± 5.4)	(3492 ± 2347)	72–101	10^4 – 10^5	7–14

^aStatistical analysis of 3 NW-FETs per sample with three gates each. Values in brackets refer to data taken under illumination.

~ 1.5 μm , giving a gate-drain distance (L_{G-D}) of ~ 300 – 700 nm depending on the accuracy of alignment (see Methods). A representative SEM image of the as-fabricated device is shown in Figure 3(a) together with a schematic of the device structure (Figure 3(b)). This device geometry enables measurement of the intrinsic NW properties via 4-terminal (4T) measurements (contacts 1–4) while also enabling the local transport and transistor characteristics to be measured at different positions along the NW by the different gates (gates A–C) (see Methods for measurement details). 4T measurements at 300 K yielded typical intrinsic NW resistances of $R_{NW} \sim 16$ – 30 k Ω , whereas the respective contact resistances ($R_C \sim 22$ – 45 k Ω) were only slightly larger, consistent for both investigated samples with differing Al-content (see also Table 1).^{26,27}

Low temperature (4.2 K) measurements revealed very different behaviors between the A and B samples. First, the intrinsic NW resistance R_{NW} decreased more than 2-fold in both samples, providing direct evidence for the formation of a confined free electron gas remote from ionized impurities. Interestingly, devices fabricated from sample B ($x(\text{Al}) = 0.25$) only exhibited a measurable low-temperature conductance after being illuminated (see Supporting Information, Figure S3). This observation is attributed to the low-temperature persistent photoconductivity (PPC) effect by which trapped charge carriers are activated upon illumination; PPC has been widely seen in planar Si δ -doped GaAs-AlGaAs 2DEG heterostructures.⁴⁴ The origin of the carrier trap state is an isolated,

elastically distorted Si donor state (so-called DX center) in the AlGaAs that occurs for Al contents higher than $x(\text{Al}) > 0.22$.^{44,45} As expected, the PPC effect was therefore negligible in sample A due to the lower Al content of $x(\text{Al}) = 0.15$, as evidenced by the nearly identical intrinsic NW resistances at 4.2 K when measured with and without illumination (see Table 1). Therefore, the following discussion of low-temperature transport investigations focuses on sample A to consider transport parameters unobscured by trap states.

We utilized the multigated NW-FET structure to spatially probe the 2DEG density and electron mobility along individual NWs and identified the influences of nanowire diameter and crystal structure. In Figure 3, the transfer characteristics (I_{SD} – V_G at $V_{SD} = 5$ mV) are shown for sample A ($x(\text{Al}) = 0.15$) at 300 K (c) and 4.2 K (d). These were conducted under bidirectional sweeps of V_G at a given gate electrode while floating the other gates to avoid their influence on the intrinsic transconductance. At both 4.2 and 300 K, no gate hysteresis is observed, indicative of excellent electrostatic gate coupling and a low-density of interface charge states between gate and channel. Also, gate leakage currents are 2 orders of magnitude smaller than the measured off-state current (see Supporting Information, Figure S4) and therefore do not notably influence the transistor characteristics. The transfer curve at 4.2 K shows a much steeper turn-on characteristic than the curve at 300 K, reflecting a much higher transconductance as expected from the thermal distribution of carriers at low temperature. Importantly,

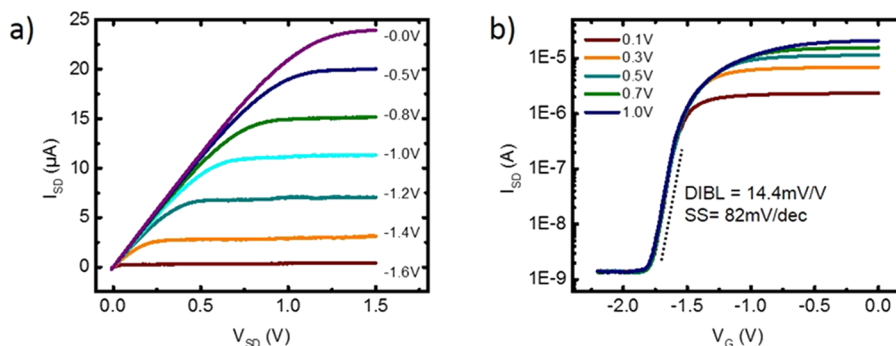


Figure 4. NW-FET characteristics at room-temperature. (a) dc (I_{SD} – V_{SD}) output characteristics under variable gate voltage V_G and (b) I_{SD} – V_G transfer characteristics under variable source-drain voltage V_{SD} for a typical Si δ -doped GaAs–AlGaAs core–shell NW-FET (sample B); SS and DIBL are 82 mV/dec and 14 mV/V, respectively. All data were measured at room-temperature.

it is worth noting that an increased on-current is also observed compared to 300 K (see Figure S4, Supporting Information), which is direct proof of high-mobility 2DEG formation at low temperature.

Very interestingly, we found that the threshold voltage V_{th} shifts consistently toward lower values when going from gate A to gate C (i.e., from the top to bottom end of the NW). To identify the origin of this trend, we considered possible changes in the respective 2DEG density along the length of the NW, because the density is directly related to V_{th} via $n_{2DEG} = C |V_{T1}| / leA$. Here, C is the gate capacitance, l is the channel length, e is the electron charge, and A is the circumference of the channel at the core–shell interface as given by the core diameter. Though the channel length is fixed, the NW core diameter varies from 90 to 25 nm from the top to bottom end of the NW, and the area into which the 2DEG is confined decreases by nearly a factor of 4. The gate capacitance C is also dependent on the NW core diameter ($C \sim 0.11$ – 0.18 fF, see Supporting Information, Figure S5). As a result, the derived 2DEG density is approximately constant along the entire length of the NW ($n_{2DEG} \sim 6.9$ – $7.7 \times 10^{11} \text{ cm}^{-2}$) and is independent of temperature as shown in Figure 3(f). This further indicates that Si doping is very homogeneous along the full length of the NW, illustrating that incorporation is dominated by direct impingement, as expected from the very low Si adatom diffusivity under the low growth temperature conditions. Moreover, it is important to note that the measured 2DEG densities are quantitatively in good agreement with the calculated (weighted) densities based on the self-consistent Schrödinger–Poisson solutions (see Figure 2 and Supporting Information). This highlights the excellent doping efficiency of the Si δ -doped layer in our remotely doped GaAs–AlGaAs core–shell NW heterostructures.

To derive the electron field-effect mobility at different positions along the NW, we determined the peak transconductance g_m [dI_{SD}/dV_G] for the three respective gates, which vary between 0.8 and 1.2 μS as shown in Figure 3(e). Note that the low-temperature g_m shows multiple distinct peaks (conductance fluctuations) arising from step-like variations in subthreshold slope directly visible in Supporting Information Figure S4b. The step-structure may arise from (i) non-concentric gate geometry and nonuniform channel depletion and (ii) distinct superposed electron channels at the corner facets that exhibit higher electron concentrations. Indeed, gate-dependent simulations (Supporting Information, Figure S6) show that depletion of the electron channel in the corner facets requires slightly higher negative bias as opposed to electron

channels residing on the side facets. This is an additional indicator for the likely superposition of 1D- and 2D-like transport channels in such hexagonally shaped wire systems.^{33,42,43}

Using the relationship $\mu = l^2 g_m / CV_{SD}$, the resulting electron field-effect mobility is plotted in Figure 3(f) as a function of NW core radius (blue data points). We note two remarkable features: first, we observe that the electron mobility increases from a few hundred $\text{cm}^2 \text{ V}^{-1} \text{ s}^{-1}$ at 300 K to ~ 4 – $5 \times 10^3 \text{ cm}^2 \text{ V}^{-1} \text{ s}^{-1}$ at 4.2 K, as expected for the free electron gas besides phonon scattering contributions from ionized impurity scattering are reduced when carriers localize in the core at low temperature. Although the extracted field-effect mobilities are much higher than those in unpassivated GaAs NW-FETs,^{28,29} they are still far below the best 2DEG mobilities realized in optimized planar Si delta-doped (110) GaAs–AlGaAs heterostructures.⁴⁶ We believe that this is likely the result of a not yet optimized dopant concentration and spacer layer thickness, as well as potential variations due to compositional fluctuations in the AlGaAs shell and corner facets.³⁷

Interestingly, the low-temperature electron mobility is also higher in devices measured toward the bottom part of the NW, where the core is smaller. We found from high-resolution TEM (Supporting Information, Figure S1) that the top (wider) region of the NW is heavily disturbed by stacking faults and twin defects, whereas the majority of the remaining narrower part of the NW consists of a phase-pure ZB crystal structure with a low density of twin defects. The variations in defect density correlate well with the lower observed electron mobility at the top, wider end of the NW, and the overall higher (~ 3 -fold larger) mobility along the major, thinner region of the NW. Hence, it is most likely that the changes in the low-temperature electron mobility are governed by microstructural variations along the NW, such as stacking faults that have been shown to dramatically influence electron scattering in other III–V-based NWs.^{47,48}

Finally, to demonstrate the improved functionality of the remote doping strategy, we characterized the dc output and transfer characteristics of these NW-FETs more closely at room-temperature. Panels a and b of Figure 4 show the dc output (I_{SD} – V_{SD} at fixed gate voltage V_G) and transfer (I_{SD} – V_G at fixed source-drain voltage V_{SD}) characteristics of a typical δ -doped GaAs–AlGaAs core–shell NW-FET (sample B). In Figure 4(a), I_{SD} – V_{SD} is measured between contacts 2–3 with V_G applied to gate B, which is varied from 0 to -1.6 V in steps of -0.2 V. The device exhibits excellent drain current saturation for all gate voltages and a shift of the threshold for saturation to

lower V_{SD} with increasingly negative V_G , demonstrating n-type conduction. More specifically, the device is an n-type depletion mode NW-FET,¹³ because it is normally on at $V_G = 0$ V (similar to all investigated devices, compare to Figure 3) and only transitions to the off-state (pinch-off) at $V_G < -1.8$ V, as seen by the switching behavior in Figure 4(b). The threshold voltage $V_T = -1.8$ V is extracted by a linear extrapolation from the point of the highest transconductance (at $V_{SD} = 1$ V). This device exhibits a steep subthreshold slope ($SS = dV_G/d[\log(I_{SD})]$) of 82 mV/dec, which compares favorably with the best switching characteristics ever reported in any of the III–V NW-FETs investigated to date.^{19–21} The on/off current ratio (I_{ON}/I_{OFF}) of this device is $>10^4$ (at $V_{SD} = 1$ V), whereas the drain-induced barrier lowering (DIBL) that is characteristic of short-channel effects is as low as 14 mV/V. Measurements on the other two gates (A,C) as well as in other NW-FETs from both samples A and B yielded similar metrics (see Table 1 and the Supporting Information). The best device metrics as measured across both samples A and B exhibited a record low SS of 70 mV/dec, I_{ON}/I_{OFF} ratio as high as $\sim 10^5$, and a record low DIBL of 7 mV/V at room-temperature (see Supporting Information).

In summary, we unambiguously demonstrated the formation of a well-confined free electron gas and resulting enhancements in electron mobility and transistor characteristics in remotely Si δ -doped GaAs–AlGaAs core–shell NW-FETs. These successes are a direct result of the powerful control over dopant incorporation and efficiency, free electron gas density, and transconductance enabled by cross-correlated atom probe tomography, band profile calculations, and low-temperature transport characterization via sophisticated omega-gate geometries with excellent electrostatic control. The as-fabricated n-channel NW-FETs exhibit remarkably good switching characteristics close to the theoretical limit (60 mV/dec) and excellent dc current saturation. The presented III–V-based high-mobility core–shell NW-FET is thus ultimately very attractive for future scaled transistors and ballistic FET devices, because the conductive channel is strongly confined to the core, inhibiting detrimental surface scattering. Further improvements in charge carrier mobility, on-current, and downscaling the gate length to the sub-50 nm regime may thus allow for important developments in future CMOS logic circuit applications. Moreover, demonstration of the confined electron gas in these 1D-like structures is expected to further enable interesting mesoscopic studies of conductance quantization (e.g., via gated quantum point contacts as well as magnetotransport investigations).

Methods. *GaAs–Al_xGa_{1–x}As core–shell Nanowire Growth.* The NWs were grown using a solid-source Veeco GEN II MBE system equipped with standard effusion cells for Ga, Al, and Si as well as a valved cracker source for the supply of As₄. As substrates, we used Si(111) wafers coated with 20 nm-thick SiO₂ that was prepatterned by nanoimprint lithography and subsequent reactive ion etching to feature periodic mask openings (pitch of 250 nm, opening size of 80 nm)⁴⁹ for site-selective growth of NW arrays. First, self-catalyzed GaAs NW cores were grown for 4 h at temperature $T = 610$ °C (as measured by optical pyrometer) using a Ga flux of 0.025 nm/s and As flux of 0.10 nm/s.⁵⁰ Prior to shell growth, the As flux was increased to 1.9 nm/s to consume the Ga droplet on the [111]-oriented growth front. The subsequent radial shell growth along the {110}-oriented sidewall facets was performed at $T = 490$ °C using Ga and As fluxes of 0.17 and 1.9 nm/s,

respectively, to mimic optimized conditions for high-quality (110) GaAs–AlGaAs heterostructures.³⁸ Shell growth was initiated by a 5 nm-thick GaAs layer to ensure a high-quality epitaxial interface between core and shell, followed by an AlGaAs spacer layer of 20 nm thickness. Growth was then interrupted, and Si was supplied for 10 min under As flux of 1.9 nm/s (δ -doped layer). Afterward, AlGaAs growth resumed to form a 60 nm-thick barrier before capping with a final 10 nm-thick GaAs cap layer. Two samples with different Al content $x(\text{Al})$ in the AlGaAs were grown, where the respective Al fluxes were set to 0.03 nm/s (for $x(\text{Al}) = 0.15$) and 0.057 nm/s (for $x(\text{Al}) = 0.25$). The entire growth procedure was performed under constant substrate rotation (5 rpm). A reference sample was also grown for APT analysis, which requires a total core–shell NW diameter of <150 nm. Here, growth was performed under identical conditions except for a slightly higher Al flux (0.072 nm/s) yielding $x(\text{Al}) = 0.3$. For this sample, the AlGaAs spacer and barriers were grown to thicknesses of 5 and 15 nm, respectively.

Structural Characterization and Dopant Profiling. Conventional transmission electron microscopy (200 kV Jeol 2011) was performed on individual NWs drop-cast onto carbon-coated copper grids to identify the crystal phase and defect composition along the NW length (see Supporting Information). An FEI Titan 80 operating at 300 kV was used for cross-sectional HAADF-STEM analysis. Here, a ~ 100 nm thin lamella was prepared from NWs (sample B) transferred onto a Ti/Au-coated glass substrate using a focused ion beam (FIB) system (Zeiss NVision 40). NWs were embedded in a carbon film to prevent damage during ion milling, followed by FIB cutting perpendicular to the growth axis, and further milling after the lamella was glued onto a Cu grid. Z-contrast imaging and energy-dispersive X-ray spectroscopy (EDXS) mapping were used to analyze the composition within the bulk and corner regions of the AlGaAs shell of sample B. EDXS analysis confirmed the expected Al-content of $x(\text{Al}) = 0.25$ in the bulk region of the AlGaAs shell, whereas the $x(\text{Al})$ was twice as large in the corner facets as reported previously.³⁷

For the atom probe tomography (APT) studies, a NW was removed from the growth substrate by nanomanipulators and attached to a tungsten probe tip by electron beam-induced metal deposition. APT was performed with a Cameca local electrode atom probe (LEAP) 4000X Si with 355 nm wavelength laser using 0.1 pJ pulse energy, 250 kHz pulse frequency, 23 K background temperature, and 0.2% target detection rate. Quantitative calibration of the reconstruction was performed by IVAS software. A spatial distribution map (SDM) was generated along the [111] direction in the (111) pole region, and the reconstruction parameters were adjusted to match the observed (111) interplanar spacing with the theoretical value of 3.26 Å. Detailed methods for generating the 2-D and 1-D composition profiles shown in Figure 1(c,d) are described in the Supporting Information.

NW-FET Device Fabrication and Measurement. To fabricate omega-gated NW-FETs in a planar geometry, the Si δ -doped GaAs–AlGaAs core–shell NWs were first removed ultrasonically from the growth substrate and drop-cast onto n^{++} -doped Si wafer pieces coated with 200 nm-thick SiO₂. In a first electron beam lithography (EBL) step, four individual source and drain contacts were defined to each NW. Before applying the contact metal, the samples were cleaned in a plasma ashing step, and the native oxide was removed in a diluted HCl solution (1:2 HCl/H₂O) for 30 s. The contact

metals for the source/drain contacts consist of AuGe/Ni/Ti/Au (50/13.6/100/290 nm) in which AuGe has a volume content of 12% Ge. To contact the 2DEG at the core-shell interface, the contacts were annealed for 90 s at 370 °C (for $x(\text{Al}) = 0.15$) and 390 °C (for $x(\text{Al}) = 0.25$). In a second EBL step, the gate structures were applied, consisting of Ti/Au (20/200 nm). Likewise, the sample was cleaned, and the native oxide was etched prior to the second metallization step. To enable electrical measurements of the fabricated devices, we glued the individual wafer pieces and bonded them to custom-designed chip carriers.

Electrical device characterization was performed at room temperature (300 K) as well as at liquid He temperature (4.2 K) using a homemade sample stick with 24 contacts. For measurements at 300 K, the sample stick was mounted in an evacuated cryostat, whereas for measurements at 4.2 K, the cryostat was further introduced into a liquid He dewar. To conduct 4-terminal measurements, a dc voltage (V_{SD}) was applied at contact 1, and the current running through the nanowire (I_{SD}) was measured at contact 4. The voltage drop due to the intrinsic resistance of the NW (V_{NW}) was thus measured at contacts 2 and 3. For 2-terminal measurements of the dc output and transfer characteristics, only two adjacent source/drain contacts were used, whereas V_{G} was applied to the gate in between. To investigate the position-dependent transfer characteristics (electron density and mobility) along the NW axis, the current was probed just as described for 4-terminal measurements, and the gate voltage (V_{G}) was applied to one of the three gates. During these measurements, the other two respective gates were kept floating.

■ ASSOCIATED CONTENT

■ Supporting Information

TEM analyses, 2D and 1D APT composition profiles and calculations, conduction band profiles, electron density maps, persistent photoconductivity effects, gate leakage data, gate capacitance calculations, and transfer characteristics. The Supporting Information is available free of charge on the ACS Publications website at DOI: 10.1021/acs.nanolett.5b00518.

■ AUTHOR INFORMATION

Corresponding Authors

*E-mail: Stefanie.Morkoetter@wsi.tum.de.

*E-mail: Gregor.Koblmueeller@wsi.tum.de.

Notes

The authors declare no competing financial interest.

■ ACKNOWLEDGMENTS

We gratefully acknowledge financial support from the German Science Foundation (DFG) via SFB 631, the Nanosystems Initiative Munich, the TUM-IAS Focus group "Nanophotonics", and the TUM International Graduate School for Science and Engineering (IGSSE). This work was also supported by the EU FP 7 project SOLID and the German Academic Exchange Service (DAAD). The authors further thank M. Bichler and P. Weiser for experimental and S. Birner and M. Falkowski for theoretical support. L.J.L. and N.J. acknowledge NSF DMR-1306854 for support.

■ REFERENCES

- (1) Dingle, R.; Störmer, H. L.; Gossard, A. C.; Wiegmann, W. *Appl. Phys. Lett.* **1978**, *33*, 665–667.
- (2) Abstreiter, G.; Ploog, K. *Phys. Rev. Lett.* **1979**, *42*, 1308.
- (3) Wang, W. I.; Mendez, E. E.; Stern, F. *Appl. Phys. Lett.* **1984**, *45*, 639–641.
- (4) Abstreiter, G.; Brugger, H.; Wolf, T.; Jorke, H.; Herzog, H. J. *Phys. Rev. Lett.* **1985**, *54*, 2241–2444.
- (5) Pfeiffer, L.; West, K. W.; Störmer, H. L.; Baldwin, K. W. *Appl. Phys. Lett.* **1989**, *55*, 1888–1890.
- (6) Ismail, K.; Arafa, M.; Saenger, K. L.; Chu, J. O.; Meyerson, B. S. *Appl. Phys. Lett.* **1995**, *66*, 1077–1079.
- (7) Klitzing, K.; Dorda, G.; Pepper, M. *Phys. Rev. Lett.* **1980**, *45*, 494–497.
- (8) Tsui, D. C.; Störmer, H. L.; Gossard, A. C. *Phys. Rev. Lett.* **1982**, *48*, 1559–1562.
- (9) Delagebeaudeuf, D.; Linh, N. T. *IEEE Trans. Electron Devices* **1982**, *29*, 955–960.
- (10) Ismail, K.; Chu, J. O.; Arafa, M. *IEEE Electron Device Lett.* **1997**, *18*, 435–437.
- (11) Petta, J. R.; Johnson, A. C.; Taylor, J. M.; Laird, E. A.; Yacoby, A.; Lukin, M. D.; Marcus, C. M.; Hanson, M. P.; Gossard, A. C. *Science* **2005**, *309*, 2180–2184.
- (12) de Picciotto, R.; Stormer, H. L.; Pfeiffer, L. N.; Baldwin, K. W.; West, K. W. *Nature* **2001**, *411*, 51.
- (13) Crook, R.; Prance, J.; Thomas, K. J.; Chorley, S. J.; Farrer, I.; Ritchie, D. A.; Pepper, M.; Smith, C. G. *Science* **2006**, *312*, 5778.
- (14) Miao, X.; Zhang, C.; Li, X. *Nano Lett.* **2013**, *13*, 2548.
- (15) Lauhon, L. J.; Gudiksen, M. S.; Wang, D.; Lieber, C. M. *Nature* **2002**, *420*, 57–61.
- (16) Xiang, J.; Lu, W.; Hu, Y.; Wu, Y.; Yan, H.; Lieber, C. M. *Nature* **2006**, *441*, 489–493.
- (17) del Alamo, J. A. *Nature* **2011**, *479*, 317–323.
- (18) Ionescu, A. M.; Riel, H. *Nature* **2011**, *479*, 329–337.
- (19) Thelander, C.; Rehnstedt, C.; Fröberg, L. E.; Lind, E.; Mårtensson, T.; Caroff, P.; Löwgren, T.; Ohlsson, B. J.; Samuelson, L.; Wernersson, L.-E. *IEEE Trans. Electron Devices* **2008**, *55*, 3030–3036.
- (20) Gu, J. J.; Wang, X. W.; Wu, H.; Shao, J.; Neal, A. T.; Manfra, M. J.; Gordon, R. G.; Ye, P. D. *IEEE Electron Device Lett.* **2012**, *33*, 967–969.
- (21) Tomioka, K.; Yoshimura, M.; Fukui, T. *Nature* **2012**, *488*, 189–192.
- (22) Jiang, X.; Xiong, Q.; Nam, S.; Qian, F.; Li, Y.; Lieber, C. M. *Nano Lett.* **2007**, *7*, 3214–3218.
- (23) Lu, W.; Xiang, J.; Timko, B. P.; Wu, Y.; Lieber, C. M. *Proc. Natl. Acad. Sci. U.S.A.* **2005**, *102*, 10046–10051.
- (24) Nah, J.; Dillen, D. C.; Varahramyan, K. M.; Banerjee, S. K.; Tutuc, E. *Nano Lett.* **2012**, *12*, 108–112.
- (25) Dillen, D. C.; Kim, K.; Liu, E.-S.; Tutuc, E. *Nat. Nanotechnol.* **2014**, *9*, 116–120.
- (26) Spirkoska, D.; Fontcuberta i Morral, A.; Dufouleur, J.; Xie, Q.; Abstreiter, G. *Phys. Status Solidi RRL* **2011**, *5*, 353–355.
- (27) Wirths, S.; Mikulics, M.; Heintzmann, P.; Winden, A.; Weis, K.; Volk, C.; Sladek, K.; Demarina, N.; Hardtgen, H.; Grützacher, D.; Schäfers, T. *Appl. Phys. Lett.* **2012**, *100*, 04210.
- (28) Bao, X.-Y.; Soci, C.; Susac, D.; Bratvold, J.; Aplin, D. P. R.; Wei, W.; Chen, C.-Y.; Dayeh, S. A.; Kavanagh, K. L.; Wang, D. *Nano Lett.* **2008**, *8*, 3755–3760.
- (29) Han, N.; Wang, F.; Hou, J. J.; Xiu, F.; Yip, S.-P.; Hui, A. T.; Hung, T. F.; Ho, J. C. *ACS Nano* **2012**, *6*, 4428–4433.
- (30) Jadczak, J.; Plochocka, P.; Mitoglu, A.; Breslavetz, I.; Royo, M.; Bertoni, A.; Goldoni, G.; Smolenski, T.; Kossaki, P.; Kretinin, A.; Shtrikman, H.; Maude, D. K. *Nano Lett.* **2014**, *14*, 2807.
- (31) Joyce, H. J.; Parkinson, P.; Jiang, J.; Docherty, C. J.; Gao, Q.; Tan, H. H.; Jagadish, C.; Herz, L. M.; Johnston, M. B. *Nano Lett.* **2014**, *14*, 5989.
- (32) Boland, J. L.; Conesa-Boj, S.; Parkinson, P.; Tütüncüoğlu, G.; Matteini, F.; Rüffer, D.; Casadei, A.; Amaduzzi, F.; Jabeen, F.; Davies,

C. L.; Joyce, H. J.; Herz, L. M.; Fontcuberta i Morral, A.; Johnston, M. B. *Nano Lett.* **2015**, *15*, 1336–1342.

(33) Funk, S.; Royo, M.; Zardo, I.; Rudolph, D.; Morkötter, S.; Mayer, B.; Becker, J.; Bechtold, A.; Matich, S.; Döblinger, M.; Bichler, M.; Koblmüller, G.; Finley, J. J.; Bertoni, A.; Goldoni, G.; Abstreiter, G. *Nano Lett.* **2013**, *13*, 6189.

(34) Lucot, D.; Jabeen, F.; Harmand, J.-C.; Patriarche, G.; Giraud, R.; Faini, G.; Mailly, D. *Appl. Phys. Lett.* **2011**, *98*, 142114.

(35) Sladek, K.; Klinger, V.; Wensorra, J.; Akabori, M.; Hardtdegen, H.; Grützmacher, D. *J. Cryst. Growth* **2010**, *312*, 635.

(36) Rudolph, D.; Hertenberger, S.; Bolte, S.; Paosanthong, W.; Spirkoska, D.; Döblinger, M.; Bichler, M.; Finley, J. J.; Abstreiter, G.; Koblmüller, G. *Nano Lett.* **2011**, *11*, 3848–3854.

(37) Rudolph, D.; Funk, S.; Döblinger, M.; Morkötter, S.; Hertenberger, S.; Scheickert, L.; Becker, J.; Matich, S.; Bichler, M.; Spirkoska, D.; Zardo, I.; Finley, J. J.; Abstreiter, G.; Koblmüller, G. *Nano Lett.* **2013**, *13*, 1522–1527.

(38) Fischer, F.; Grayson, M.; Schuberth, E.; Schuh, D.; Bichler, M.; Abstreiter, G. *Phys. E* **2004**, *22*, 108–110.

(39) Perea, D. E.; Allen, J. E.; May, S. J.; Wessels, B. W.; Seidman, D. N.; Lauhon, L. J. *Nano Lett.* **2006**, *6*, 181.

(40) Perea, D. E.; Hemesath, E. R.; Schwalbach, E. J.; Lensch-Falk, J. L.; Voorhees, P. W.; Lauhon, L. J. *Nat. Nanotechnol.* **2009**, *4*, 315–319.

(41) Birner, S.; Zibold, T.; Andlauer, T.; Kubis, T.; Sabathil, M.; Trellakis, A.; Vogl, P. *IEEE Trans. Electron Devices* **2007**, *54*, 2137–2142.

(42) Ferrari, G.; Goldoni, G.; Bertoni, A.; Cuoghi, G.; Molinar, E. *Nano Lett.* **2009**, *9*, 1631–1635.

(43) Bertoni, A.; Royo, M.; Mahawish, F.; Goldoni, G. *Phys. Rev. B* **2011**, *84*, 205323.

(44) Mooney, P. M. *Appl. Phys. Rev.* **1990**, *67*, R1.

(45) Chand, N.; Henderson, T.; Klem, J.; Masselink, W. T.; Fischer, R.; Chang, Y.-C.; Morkoc, H. *Phys. Rev. B* **1984**, *30*, 4481.

(46) Fischer, F.; Grayson, M.; Schubert, E.; Schuh, D.; Bichler, M.; Abstreiter, G. *Phys. E* **2004**, *22*, 108.

(47) Schroer, M. D.; Petta, J. R. *Nano Lett.* **2010**, *10*, 1618–1622.

(48) Sourribes, M. J. L.; Isakov, I.; Panfilova, M.; Liu, H.; Warburton, P. A. *Nano Lett.* **2014**, *14*, 1643–1650.

(49) Hertenberger, S.; Funk, S.; Vizbaras, K.; Yadav, A.; Rudolph, D.; Becker, J.; Bolte, S.; Döblinger, M.; Bichler, M.; Scarpa, G.; Lugli, P.; Zardo, I.; Finley, J. J.; Amann, M.-C.; Abstreiter, G.; Koblmüller, G. *Appl. Phys. Lett.* **2012**, *101*, 043116.

(50) Rudolph, D.; Schweickert, L.; Morkötter, S.; Loitsch, B.; Hertenberger, S.; Becker, J.; Bichler, M.; Abstreiter, G.; Finley, J. J.; Koblmüller, G. *Appl. Phys. Lett.* **2014**, *105*, 033111.